2026 IEEE International Conference on Robotics and Automation (ICRA 2026)
June 1-5, 2026. Vienna, Austria

Design of an Untethered Multi-Mode Swimming Robot Driven by Electromagnetic Actuators

Jinchun Yan[1], Yiyi Lu[1], Qifan Li[1], and Oncay Yasa[1,2,*]

***Abstract*— Underwater robots have significant potential for a wide range of applications, including deep-sea exploration, hydrocarbon extraction, marine biodiversity observation, and waste retrieval. A hybrid actuation system that combines electromagnets and permanent magnets preserves the main benefits of magnetic-driven robots, addressing the issues of bulky coil systems and limited mobility. However, most electromagnetically actuated underwater robots are limited to a fixed swimming mode due to their relatively simple designs, which restrict their adaptability to unpredictable and unstructured aquatic environments. In this work, we present an untethered multi-mode swimming robot driven by four 2-degrees-of-freedom (DoF) electromagnetic actuators, each with a rigid shell interconnected by flexible connectors and covered with silicone membranes. Initially, we conducted tests to determine the optimal hardness of the flexible connector by validating the module's range of motion across different activation times. Next, we demonstrated that the robot can swim forward and backward in a water tank, exhibiting snake-inspired motion, front- and rear-undulation, and wave-shaped motion, and reaching a maximum speed of $87.8\ \mathrm{mm\,s^{-1}}$. Finally, we showed the lateral translation and steering motions achieved with different control signals, resulting in an average turning speed of $3\,^{\circ}\,\mathrm{s^{-1}}$. This approach enables a novel robot design strategy based on compact multi-DoF electromagnetic modules, facilitating potential applications in search-and-rescue missions and environmental inspections.**

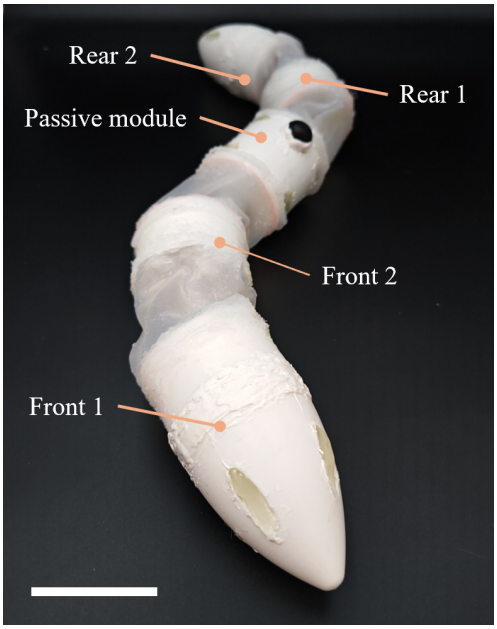

Fig. 1. The untethered multi-mode swimming robot that has four 2-DoF electromagnetic modules (*i.e.*, Front 1 & 2 and Rear 1 & 2) and one passive module, which houses the electronics. The scale bar represents $50\ \mathrm{mm}$.

I. INTRODUCTION

Multimodal locomotion robots, capable of adapting to different environments by changing their motion behaviors, such as swimming, crawling, walking, and jumping, have potential for use in unstructured and dynamic environments [1]–[3]. Meanwhile, oceans play an important role due to their rich marine resources, making it essential to develop underwater robots for environmental monitoring, interacting with marine life with minimal disturbance, and search and rescue missions [4], [5]. Particularly, swimming locomotion is a type of powerful and effective motion behaviors, thereby attracting researchers to design swimming robots with various actuation methods, including pneumatics [6]–[8], hydraulics [9]–[11], electrohydraulics [12]–[14], electrics [15]–[17], magnetics [18], [19], dielectric elastomers [20], and eletromagnetics [21], [22].

Conventional underwater robots are typically composed of rigid components, such as traditional motors, which can provide stable and adequate operation. Kim *et al.* introduced an underwater robot driven by waterproof servomotors, achieving swimming, walking, and crawling motions by designing a multimodal fin structure and a spine mechanism [15]. However, these robots lack the material softness and adaptability due to the inherent rigidity of their components. Soft robots are capable of deforming and safely interacting with humans and their environments, and can be actuated by external stimuli, such as electric and magnetic fields [23].

Xu *et al.* proposed a manta ray-inspired soft robot driven by pneumatic actuators, demonstrating different swimming motions such as forward/backward swimming, turning, and flip-turning [7]. Compared with pneumatic-driven soft robots, hydraulic systems can extend operating time due to their high energy efficiency and provide low- to high-frequency actuation. Liu *et al.* introduced a hydraulic-driven soft robotic fish with two active joints, completing turning, diving–floating, and long-distance continuous swimming tests [10]. Also, Park *et al.* developed a hydraulic-driven soft robotic fish with three independently controllable segments, achieving anguilliform and thunniform swimming modes by changing the flow rates and phase shift of the pumps [24]. Shi *et al.* presented a hydraulic-driven underwater soft-bodied snake robot

This work is supported by the Guangdong Basic and Applied Basic Research Foundation (No. 2025A04J3843). [1]All authors are affiliated with Biohybrid Robotics Lab, Thrust of Robotics and Autonomous Systems, The Hong Kong University of Science and Technology (Guangzhou), Guangzhou, 511453, China. [2]Oncay Yasa is also affiliated with Thrust of Bioscience and Biomedical Engineering, The Hong Kong University of Science and Technology (Guangzhou), Guangzhou, 511453, China. *Corresponding author: Oncay Yasa (*oncayyasa@hkust-gz.edu.cn*)

that has self-shape perception capability, mimicking the serpentine motion of real snakes and investigating two turning strategies [11]. To generate a large deformation with a fast response, Wang *et al.* designed a soft biomimetic robotic fish driven by multilayer columnar dielectric elastomer actuators, achieving multiple swimming modes, including *anguilliform*, *subcarangiform*, *carangiform*, and *thunniform* [20]. In addition, this robot can adapt its swimming mode according to the swimming environment by using its onboard sensors. To simplify the manufacturing process while maintaining high performance and low acoustic noise, Hartmann *et al.* presented an untethered flat robot by designing electrohydraulic-powered undulating fins, navigating through narrow spaces, pushing objects, and detecting the direction of external light sources [12]. To avoid utilizing high driving voltages, which pose a safety concern for operators, magnetic actuation is a good candidate due to its unique advantages, such as non-contact operation and rapid response. Li *et al.* proposed an untethered ray-inspired soft magnetic robot, which can realize flapping, steering, and translational motion on the water surface while collecting its inertial and temperature information in real-time for motion monitoring [19]. Although this magnetic robot is remotely controllable, its mobility is limited by the static Helmholtz coil system, as it is confined to the magnetic field workspace. Electromagnetic actuators can overcome this limitation while maintaining the benefits of magnetic actuation, which does not require mechanical connections. Wei *et al.* [21] and Hennig *et al.* [22] developed an electromagnetic-driven fish-like robot and a humanoid soft underwater robot, both incorporating permanent magnets (PMs) in their flexible tail fins to enable free swimming and steering. However, their designs limit the number of actuating elements, which hampers their ability to perform different swimming modes.

In this paper, we present an untethered multi-mode swimming robot composed of four 2-DoF modules based on electromagnetic actuators, achieving front- and rear-undulation, snake-inspired, wave-shaped, lateral translation, and turning motions (Fig. 1). By employing a symmetric arrangement of these 2-DoF electromagnetic modules, the robot can switch between five distinct swimming modes by changing the actuation signals. This symmetric design, along with hollow cylindrical permanent magnets, enables all electronics to be housed either within the electromagnetic modules or the middle passive module, accessible through holes in the magnets and silicone rubber tubes. However, the relationship between deformation and hardness in silicone rubber remains unknown. Concurrently, we analyzed the trajectories of a single module with different silicone rubber harnesses and varied actuation times of electromagnetic actuators to produce a cone-shaped range of motion. In addition, to further demonstrate its effectiveness, we measured the bending angles while changing the activation times at a constant voltage. The main contributions of this work are summarized as follows:

1) Compared with traditional motor designs, the proposed electromagnetic actuator can achieve 2-DoF motion with fast response in a compact form, enhancing the robot's maneuverability by realizing multiple swimming modes.

2) The motion direction of the robot can be switched by merely adjusting the actuation sequences due to the symmetric rigid-soft hybrid structural design.

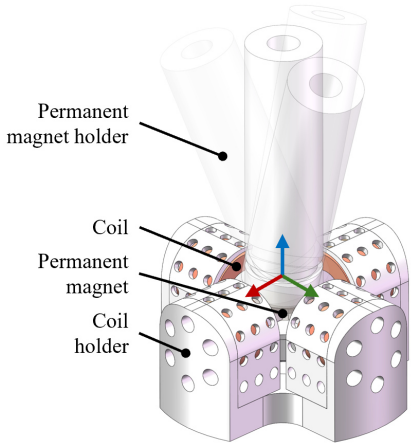

Fig. 2. The working principle of the electromagnetic module. The structure consists of a hollow permanent magnet (PM), a PM holder, a coil holder, and four coils. The red, green, and blue arrows stand for the X, Y, and Z axes, respectively.

II. ROBOT DESIGN

A. 2-DoF Electromagnetic Module Design

While the electromagnetic actuation is widely employed for underwater robots, these robots [21], [22] used a pair of coils to generate undulating motion in the plane. By mimicking the working principle of brushless DC motors, we orthogonally placed two pairs of coils, which were fixed by the coil holder (Fig. 2). We employed four coils because they can directly generate magnetic forces in two orthogonal directions, thereby simplifying the control strategy and improving its accuracy. The electromagnetic module was composed of a hollow cylindrical PM, a PM holder, a coil holder, a soft connector, and four coils. However, to illustrate the working principle, the outer shell and flexible connector of the electromagnetic actuator are not shown in Fig. 2. When the coil holder is fixed, the hollow PM with the PM holder can generate three rotational motions along the X and Y axes by controlling the amplitudes and directions of the applied currents for coils.

The design of the 2-DoF electromagnetic module based on the working principle aforementioned is shown in Fig. 3(a). To ensure a stable output force and reduce the interference caused by internal wires passing through the holes, we secured the position of the PM. This setup allows the coils to move freely along with the coil holder and the outer shell. Furthermore, leveraging the flexibility of Connector 1, composed of silicone rubber, the module is capable of executing two rotational motions. Specifically, to mitigate the uncertainty in initial orientation caused by magnetic interference with metallic components, soft connectors were engineered as replacements for traditional ball joint bearings.

To further reduce control and the number of control units, we reversed the connections between each pair of coils to enable anti-phase actuation. For example, when the lower end of Coil 1 is magnetized to the S pole, and the upper end of Coil 3 is magnetized to the N pole, this configuration attracts the module toward the central PM if the upper end of the PM is the N pole. This approach can also, in principle, boost the output magnetic force, since both coils simultaneously influence the magnet. The hollow PM was attached to Connector 2 with glue, and Connectors 1 and 2 were connected via a two-step casting process using silicone rubbers with different hardnesses, as described in the next section.

B. Materials Selection

All rigid components are made of polylactic acid (PLA) using a 3D printer. A sealing gasket was used to fill the gap between the connection parts of the shell, thereby ensuring a watertight seal. N52 grade hollow cylindrical neodymium iron boron (NdFeB) magnets with an inner diameter of 4 mm, an outer diameter of 12 mm, and a height of 5 mm were utilized due to the highest maximum energy product. The magnet with axial magnetization was fixed with the Connector 2 (Fig. 3(a)), which is made of silicone rubber with a Shore hardness of 40A. This choice is based on the

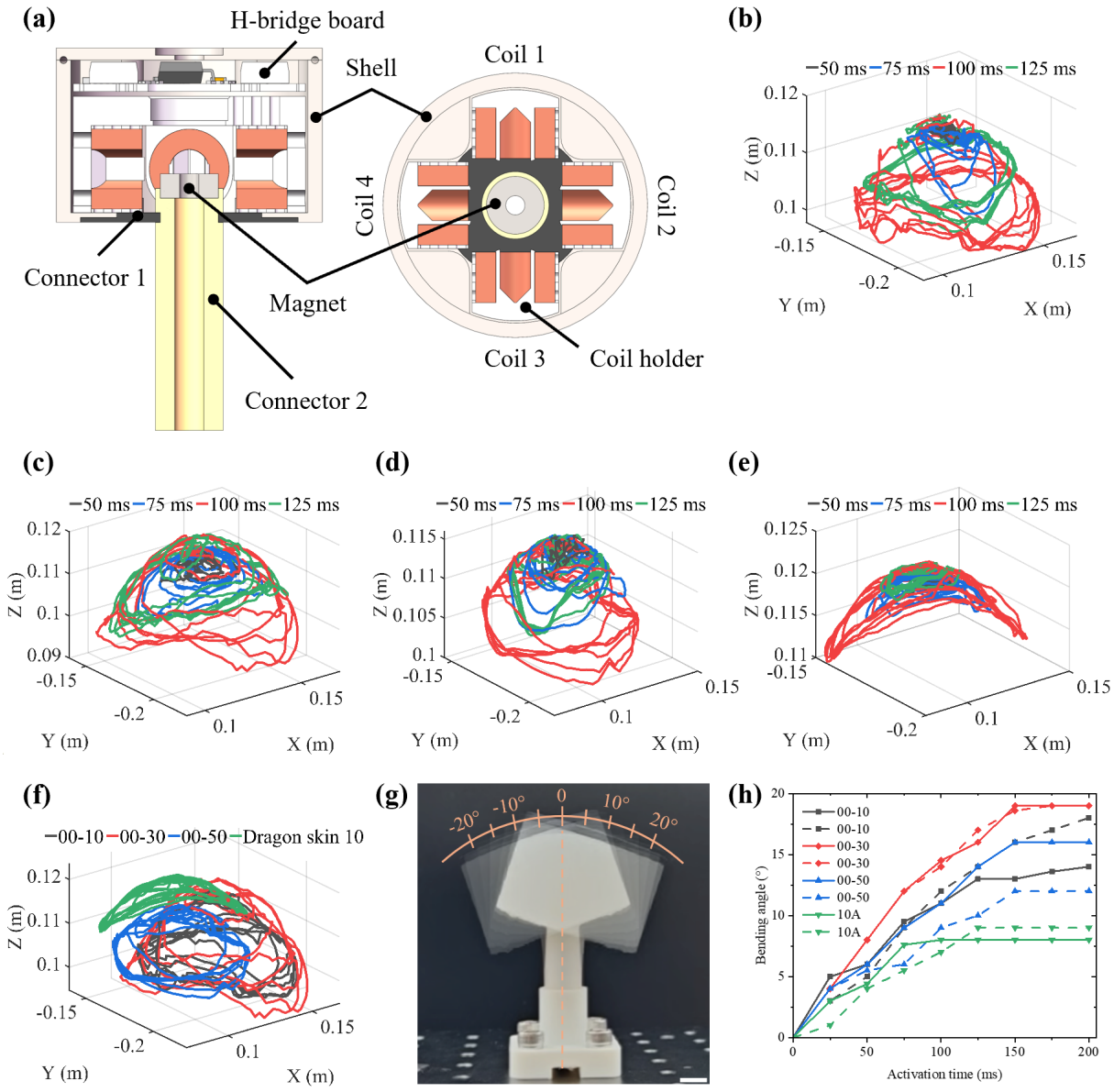

Fig. 3. Structural design and material selection. (a) The design of the entire electromagnetic module and its corresponding cross-sectional view. Trajectories with four different activation times, *i.e.*, 50 ms, 75 ms, 100 ms, and 125 ms, and Shore hardnesses, including 00-10 (b), 00-30 (c), 00-50 (d), and 10A (e). (f) The performance comparison among materials of varying hardness under the identical actuation time of 100 ms. (g) Bending angle of the module subjected to an activation time from 0 to 200 ms. (h) Quantitative analysis of the bending angle in both directions. Solid lines stand for the angle of bending to the left, while dashed lines represent the angle of bending to the right. The scale bar represents 10 mm.

fact that using a harder material can enhance the mechanical stability of the module's motion, thereby effectively mitigating bending or deformation induced by gravity. Specifically, soft segments were connected to the rigid components with silicone adhesive (*i.e.*, Sil-Poxy, Smooth-On Inc.) to ensure reliable and robust bonding.

One important design parameter of Connector 1 is its hardness. We conducted a series of tests to determine its hardness and ensure the module's overall stiffness is sufficient to optimize its range of motion during the actuation cycle, enabling the PM returns to its original state when the coils are off. Particularly, we fabricated four modules (Fig. 3(a)) from different silicone rubber elastomers (*i.e.*, Ecoflex 00-10, 00-30, 00-50, and Dragon Skin 10, Smooth-On Inc.) and fixed them to an optical table for testing their range of motion. Their motion trajectories under different actuation inputs were measured by using a motion capture system (PrimeX 22, OptiTrack). In addition, to adjust the current magnitude, we controlled the coil's activation time, setting it to four values in 25-ms increments from 50 to 125 ms. We sent signals to control the module to execute six consecutive circular motions under each activation time setting (Fig. 3(b) to (e)). The results indicate that an activation time of 100 ms can achieve an optimal performance across the selected hardness values. Moreover, we integrated all 100-ms curves (Fig. 3(f)) and calculated the corresponding projected areas. The projected area of the Ecoflex 00-30 curve is comparable to that of 00-10, albeit slightly larger.

To further compare performance differences and determine a suitable hardness, we performed bending tests using the same experimental setup. Specifically, we controlled the module to achieve one undulating direction with different activation times, ranging from 0 ms to 200 ms in increments of 25 ms (Fig. 3(g) and (h)). The results indicate that the Ecoflex 00-30 curve can achieve the largest unilateral bending deformation of 19°, with more stable bending angles observed on both the left and right sides. Although the bending angle of the module generally increases as its hardness decreases, the observed discrepancy may be attributed to the excessive softness of the material (Ecoflex 00-10), which compromises its ability to adequately support the entire module under gravity. Specifically, the module exhibits a mismatch between the bending angles in the left and right directions due to the inertia effects during its motion. The difference is also partly caused by variations in the tightness of conductive wires within the module. Therefore, we selected Ecoflex 00-30 as the material for fabricating Connector 1.

We also designed a soft skin made of silicone rubber between each module to reduce drag. However, an improperly sized membrane could interfere with the deformation of the robot. Hence, the actual length of this membrane was modeled (Fig. 4) and calculated as follows:

$$L' = L + \frac{D}{2} \cdot \alpha \cdot 2 \tag{1}$$

where L and L' are the distances between two modules at different deformation states, D is the outer diameter of the module, and α is the maximum bending angle. Substituting the actual values of these parameters (*i.e.*, L = 41 mm, D = 55 mm, α = 20°) into Equation 1 yields the expected length of 60.2 mm.

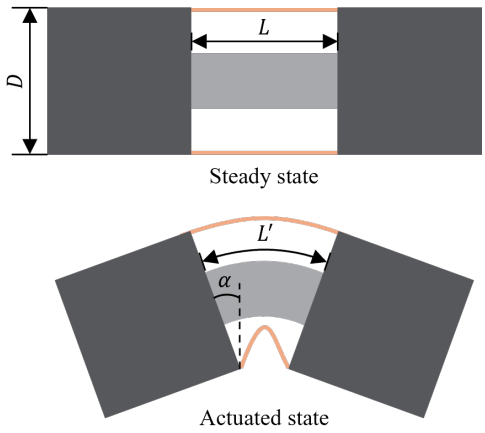

Fig. 4. Geometric descriptions used for the analysis of length changes in the silicone rubber membrane between its steady and actuated states. The light gray part represents the silicone rubber tube (*i.e.*, Connector 2), the dark gray parts stand for the electromagnetic module, and the orange parts serve as the silicone membrane.

C. Coil Validation

The parameters of the coil used in this work are as follows: the diameter of the copper wire is 0.25 mm with 500 turns; the inner/outer diameters are 8.1/15.1 mm, respectively; the height is 10 mm, and the resistance is 6.8 Ω. According to the Biot-Savart law, we can derive the equation for calculating the magnetic field at a point along the axis of a solenoid as follows:

$$B(z) = \frac{\mu_0 N I}{2h}\left[\frac{z+\frac{h}{2}}{\sqrt{a^2+\left(z+\frac{h}{2}\right)^2}} - \frac{z-\frac{h}{2}}{\sqrt{a^2+\left(z-\frac{h}{2}\right)^2}}\right] \tag{2}$$

where μ_0 is the vacuum permeability, N is the number of turns, a and h are the effective radius and the height of the coil, I is the applied current, and $B(z)$ is the magnetic field strength of axial field component at a distance of z. To obtain the magnetic field distribution generated by the coil, we utilized the Hall magnetic field camera (HallinSight Co.), which can map dynamic magnetic fields in real-time. However, these three-axis Hall sensors spacing in X-, Y-, and Z-direction is 2.5 mm. We applied 1 A and 1.6 A currents to the coil (Fig. 5(a) and (b)), generating maximum Z-axis magnetic fields are 13.75 mT and 22.9 mT, respectively, similar to the theoretical values calculated by the Equation 2 (*i.e.*, 14.2 mT and 22.7 mT when z equals to 7.5 mm).

Also, using the 11.1 V power supply, a peak current of 0.73 A is sent each time, resulting in consumption of 0.31 mWh per actuation. The coils surface will increase by approximately 60 °C (Fig. 5(c)) after operating for 180 s at 1 Hz and 158 s at 3 Hz, respectively.

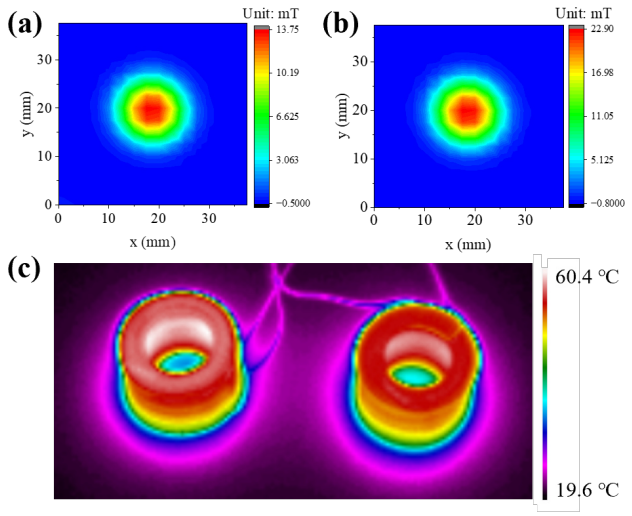

Fig. 5. The distribution and strength of the generated magnetic field when the applied current is 1 A (a) and 1.6 A (b). (c) The heatmap of a pair of coils during their actuation for 158 s at 3 Hz.

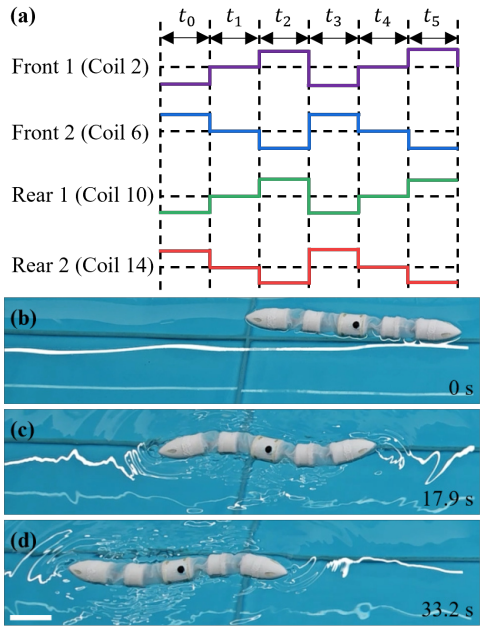

Fig. 6. Snake-inspired motion of the robot. (a) Driving signals of the four modules in the robot. Since the two coils are wired with opposite polarity, only one coil is shown as a representative for each joint in the diagram. The snapshots of the swimming motion with t = 0 s (b), 17.9 s (c), and 33.2 s (d). The scale bar represents 10 cm.

D. Electronics

The control system of the robot integrates an Arduino Nano ESP32 microcontroller with Bluetooth Low Energy (BLE), four customized dual bidirectional H-bridge boards, and a lithium battery (3S-300 mAh), enabling remote control. Specifically, one H-bridge board can actuate two pairs of coils, placed in the corresponding module, thereby enhancing compactness. Other electronics are housed in the passive module of the robot.

III. EXPERIMENTS AND RESULTS

The variety of swimming modes was explored through experiments in a water tank. First, we actuated the robot to achieve forward/backward motion, including the snake-inspired swimming, front/rear undulation, and wave-shaped motion. Next, the robot performed lateral motion and steering maneuvers to enhance its versatility by utilizing different actuation strategies. In particular, the robot, with a total length of 496 mm and a mass of around 621 g, has five modules, including four active electromagnetic modules and one passive module, thus requiring 16 coils, which are labeled as Coil 1 to Coil 16 (*i.e.*, #1 to #4 for the Front 1, #5 to #8 for the Front 2, #9 to #12 for the Rear 1, and #13 to #16 for the Rear 2) according to the definition shown in Fig. 3(a). By leveraging the robot's symmetrical design, multiple swimming modes can be accomplished through the regulation of the actuating sequences of its four active modules. Additionally, the flexible connectors were designed to store energy during the activation of the electromagnetic modules, thereby enabling the robot to return to its original position upon deactivation of these modules.

Furthermore, the battery and microcontroller were placed at the bottom of the passive module, and ballast was added to the Front 1 and Rear 2 modules, allowing the robot to float on water and stay upright without external control signals. In the following experiments, we set the activation time to 150 ms because it is the shortest time required to achieve the maximum bending deformation (Fig. 2(h)). Instead of continuously sending command signals to the robot, we used pulse signals to reduce the heat generation from the coils.

A. Snake-Inspired Motion

The sinusoidal traveling-wave equation is the most widely used strategy in the field of snake robots to achieve serpenoid undulation motions [11], [25]. Inspired by this strategy, we designed a control sequence diagram for each module to achieve a snake-inspired swimming motion (Fig. 6(a)). We demonstrated two cycles of this swimming mode as follows:

- Step 1: The front modules and rear modules are actuated simultaneously and in opposite directions to form a sinusoidal shape over a duration of t_0.
- Step 2: The robot has a time delay (t_1) related to the actuation frequency and the time required to restore the module's original position. In this context, the motion period is defined as 1 Hz.
- Step 3: Before starting the next actuation cycle (from t_3 to t_5), all modules are activated by signals that command motion in the opposite direction compared to Step 1.

By repeating this cycle, the robot successfully achieved snake-inspired swimming (Fig. 6(b), (c), and (d)). The entire motion process was recorded and analyzed by using the Tracker software, reaching a maximum velocity of 49.3 $\mathrm{mm\,s^{-1}}$ at 1 Hz.

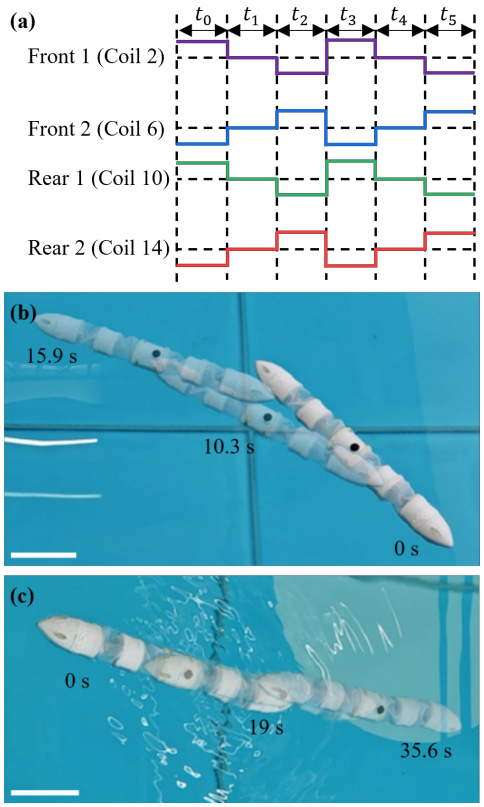

Fig. 7. Front/rear undulation motion of the robot. (a) Driving signals of the four modules in the robot. The snapshots of the forward swimming (b) with a speed of up to 69.7 $\mathrm{mm\,s^{-1}}$ at 3 Hz and backward swimming (c) with a maximum velocity of 38.5 $\mathrm{mm\,s^{-1}}$ at 1 Hz. Scale bars represent 10 cm.

B. Front/Rear Undulation Motion

The front/rear undulation motion features a large swing amplitude that propagates a bending wave rearward with a phase lag, causing the oscillation of the rear body and caudal fin [20]. By mimicking this gait, we developed a driving sequence diagram for the front and rear modules to achieve forward and backward swimming (Fig. 7(a)). Similar to the control signal used for the snake-inspired motion, including activation and stay time, we also present two cycles of this swimming mode as follows:

- Forward swimming: During t_0 and t_2, the two front modules are actuated simultaneously in opposite directions without considering the frequency-related delay time (*i.e.*, t_1).
- Backward swimming: This swimming mode can be achieved by actuating only the rear modules, allowing the front modules to remain static or serve as passive followers.

Subsequently, to evaluate the swimming robot's speed performance, we conducted experiments at actuation frequencies of 1 Hz and 3 Hz. It was observed that the forward swimming speed can reach 69.7 $\mathrm{mm\,s^{-1}}$ at 3 Hz (Fig. 7(b)) and the backward motion's velocity is around 38.5 $\mathrm{mm\,s^{-1}}$ at 1 Hz (Fig. 7(c)). Furthermore, by increasing the actuating frequency to 3 Hz, we achieved a maximum backward swimming speed of 87.8 $\mathrm{mm\,s^{-1}}$. Owing to its small body undulation, the robot employing this swimming strategy is capable of operating in confined workspaces.

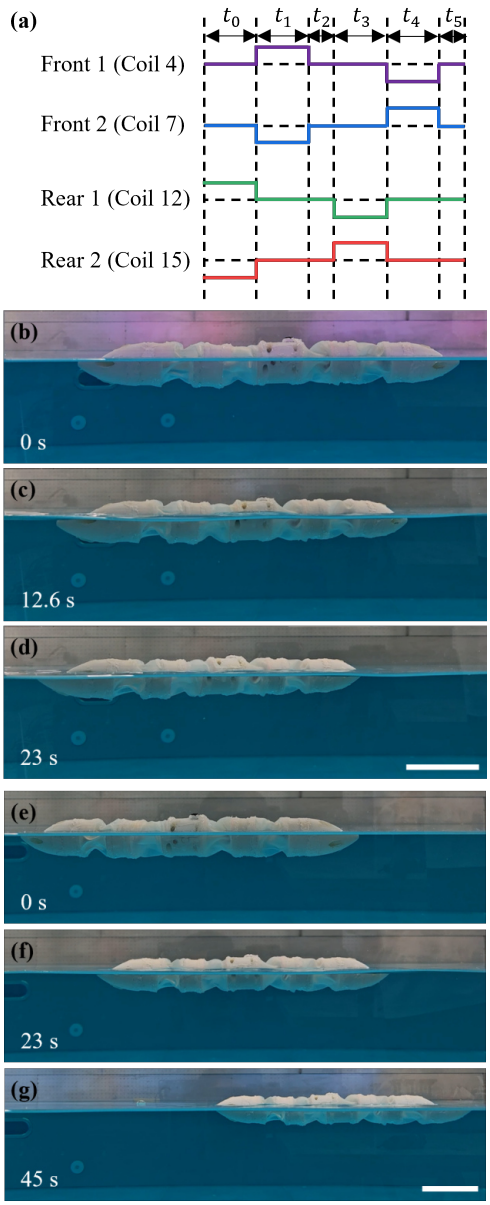

Fig. 8. Wave-shaped motion of the robot. (a) Actuating signals of the four modules in the robot. The snapshots of the robot during forward (b-d) and backward swimming motion (e-g) at selected time points. The scale bars represent 10 cm.

C. Wave-Shaped Motion

To demonstrate a key advantage of our 2-DoF electromagnetic module design, which can generate waveforms in different directions, we proposed an actuation timing diagram for each module to achieve wave-shaped swimming motion (Fig. 8(a)), a gait inspired by other robots [26], [27]. We highlight one cycle of this swimming motion as follows:

- Wave-shaped forward swimming: The first half of the cycle from t_0 to t_2 applies anti-phase signals to drive

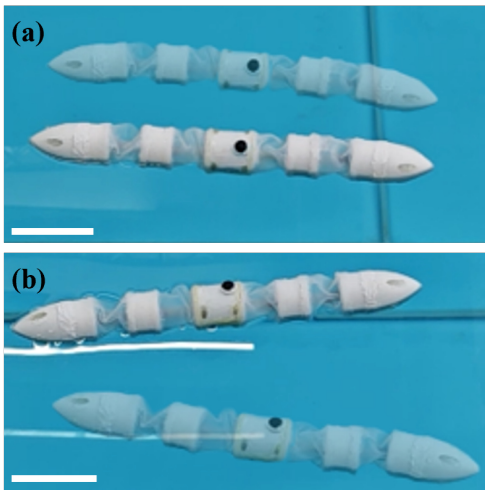

Fig. 9. Lateral translation motion of the robot. The snapshots of the lateral undulation up (a) and down (b) with two different actuation signals. The scale bars represent 10 cm.

the rear modules, immediately followed by an equivalent actuation of the front modules. Notably, t_2 is the predetermined stay time to complete the half-cycle. The next half cycle repeats this two-phase sequence with reversed signal polarities from t_3 to t_5.

- Wave-shaped backward swimming: By reversing the control sequence used for the forward swimming, the robot can generate a traveling-wave backward motion that approximates a sinusoid in the sagittal plane.

The results indicated that the wave-shaped forward motion can achieve a velocity of 38.2 $\mathrm{mm\,s^{-1}}$ at 1 Hz (Fig. 8(b), (c), and (d)) and the backward motion (Fig. 8(e), (f), and (g)) with a comparable speed (*i.e.*, 38 $\mathrm{mm\,s^{-1}}$ at 1 Hz).

D. Lateral Translation Motion

Conventional undulatory robots excel in pitch and yaw movements for moving forward, but typically cannot control their lateral translation. To extend the applicability of the robot, we investigated its lateral motion by presenting two control methods for each module (Fig. 9). The first method was to synchronize all coils on the same side, allowing the robot's lateral movement by forming a C-shaped body, achieving a maximum speed of (32.8 $\mathrm{mm\,s^{-1}}$ at 2 Hz; Fig. 9 (a)). The second method employed an anti-phase actuation of the front modules combined with sequential undulation of the rear modules, achieving a maximum speed of 40.8 $\mathrm{mm\,s^{-1}}$ at 0.77 Hz (Fig. 9 (b)). Hence, the second method is more suitable for lateral motion, as it reaches a higher speed. This advantage stems from the first method's lower speed, probably caused by using only half the available undulating stroke while operating at 2 Hz, thereby limiting its maximum velocity. Specifically, this lateral motion enhances the robot's maneuverability, enabling quieter and more stable approaches for observation missions. It also significantly improves its navigational and operational performance within confined spaces.

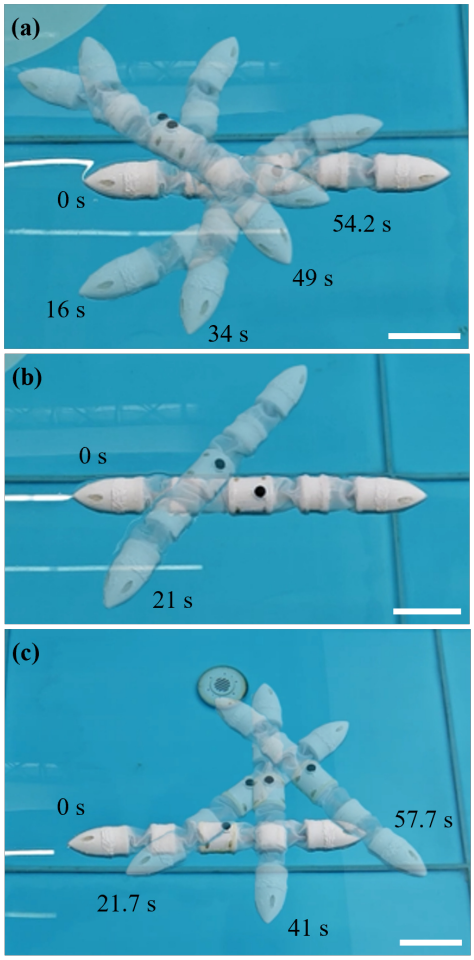

Fig. 10. Turning motion of the robot. The snapshots of the steering motion with three different actuation methods, including the front modules with 2 Hz actuation and rear modules with 1 Hz (a), the front modules with 1 Hz actuation and rear modules with 2 Hz (b), and the anti-phase actuation for the front modules and in-phase actuation for the rear modules with 0.77 Hz. The scale bars represent 10 cm.

E. Turning Motion

Although the symmetric design allows the robot to switch between forward and backward motion simply by changing the control signals, achieving steering motion with different turning angles remains a necessary and distinct capability. To achieve turning motion, we examined three different methods as follows:

- Method 1: We used the control strategy from the snake-inspired motion by varying the actuation frequency. For example, actuating the front modules with 2 Hz and the rear modules with 1 Hz (Fig. 10 (a)) resulted in an average turning speed of $3\,^\circ\,\mathrm{s^{-1}}$.
- Method 2: We controlled the front modules at 1 Hz and the rear modules at 2 Hz (Fig. 10 (b)), realizing an average turning speed of $2.43\,^\circ\,\mathrm{s^{-1}}$.
- Method 3: We used a new strategy where the front modules were actuated in anti-phase and the rear modules in in-phase during the operational cycle (Fig. 10 (c)), achieving an average turning speed of $2.37\,^\circ\,\mathrm{s^{-1}}$.

The results demonstrated that the robot's turning motion with Method 1 is faster than the other methods. This is partly because the high undulation frequency of the front modules increases the steering torque, leading to a faster turning speed. Notably, the robot may drift due to the difference in actuation frequency and water flow.

IV. CONCLUSIONS

In this work, we presented the design of an untethered electromagnetic robot having multiple swimming modes, such as three forward/backward motions, two lateral translations, and two turning maneuvers, demonstrating the effectiveness of our 2-DoF module design strategy. Specifically, the robot consists of four rigid active modules linked by soft connectors and one passive module, housing all electronics except for the H-bridge boards. Each active module features four coils with a coil holder and a hollow cylindrical permanent magnet. These modules are interconnected by soft connectors, which link the modules and support the robot. Through a series of experiments, we determined the optimal silicone rubber hardness and established the relationship between coil activation time and the resulting bending angle. Additionally, we developed a theoretical model to identify the optimal length of the silicone membrane, reducing drag force without compromising bending performance.

Concurrently, we conducted experiments to characterize the robot's lateral swimming speed and the turning agility under different actuation signals. Future work aims to improve swimming performance by further exploring the design parameters of the electromagnetic module. Although this work examined different motions using various actuation methods, integrating sensing components, such as depth sensors, inertial measurement units, and other functional modules, will enable the robot to perform practical underwater tasks, such as environmental monitoring and inspection.

REFERENCES

[1] R. Baines, S. K. Patiballa, J. Booth, *et al.*, "Multi-environment robotic transitions through adaptive morphogenesis," *Nature*, vol. 610, no. 7931, pp. 283–289, Oct. 13, 2022.

[2] A. Crespi, K. Karakasiliotis, A. Guignard, and A. J. Ijspeert, "Salamandra robotica II: An amphibious robot to study salamander-like swimming and walking gaits," *IEEE Trans. Robot.*, vol. 29, no. 2, pp. 308–320, Apr. 2013.

[3] J. Sun, E. Lerner, B. Tighe, C. Middlemist, and J. Zhao, "Embedded shape morphing for morphologically adaptive robots," *Nat. Commun.*, vol. 14, no. 1, p. 6023, Sep. 27, 2023.

[4] J. Qu, Y. Xu, Z. Li, *et al.*, "Recent advances on underwater soft robots," *Adv. Intell. Syst.*, vol. 6, no. 2, p. 2 300 299, Feb. 2024.

[5] R. Wang, C. Zhang, Y. Zhang, W. Tan, W. Chen, and L. Liu, "Soft underwater swimming robots based on artificial muscle," *Adv. Mater. Technol.*, vol. 8, no. 4, p. 2 200 962, Feb. 2023.

[6] Y. Zhai and M. T. Tolley, "Electronics-free 3d-printed soft swimming robot with pneumatic oscillating control for efficient undulating locomotion," *IEEE Robot. Autom. Lett.*, vol. 10, no. 8, pp. 7891–7898, Aug. 2025.

[7] Z. Xu, J. Liang, and Y. Zhou, "Manta ray-inspired soft robotic swimmer for high-speed and multi-modal swimming," in *2024 IEEE/RSJ International Conference on Intelligent Robots and Systems (IROS)*, IEEE, Oct. 14, 2024, pp. 235–240.

[8] H. Qing, J. Guo, Y. Zhu, *et al.*, "Spontaneous snapping-induced jet flows for fast, maneuverable surface and underwater soft flapping swimmer," *Sci. Adv.*, vol. 10, no. 49, eadq4222, Dec. 6, 2024.

[9] R. K. Katzschmann, J. DelPreto, R. MacCurdy, and D. Rus, "Exploration of underwater life with an acoustically controlled soft robotic fish," *Sci. Robot.*, 2018.

[10] S. Liu, C. Liu, G. Wei, L. Ren, and L. Ren, "Design, modeling, and optimization of hydraulically powered double-joint soft robotic fish," *IEEE Trans. Robot.*, vol. 41, pp. 1211–1223, 2025.

[11] H. Shi, Y. Meng, W. Cui, M. Rao, S. Wang, and Y. Xie, "Biomimetic underwater soft snake robot: Self-motion sensing and online gait control," *IEEE Trans. Robot.*, vol. 41, pp. 1193–1210, 2025.

[12] F. Hartmann, M. Baskaran, G. Raynaud, M. Benbedda, K. Mulleners, and H. Shea, "Highly agile flat swimming robot," *Sci. Robot.*, 2025.

[13] S.-D. Gravert, E. Varini, A. Kazemipour, *et al.*, "Low-voltage electrohydraulic actuators for untethered robotics," *Sci. Adv.*, vol. 10, no. 1, eadi9319, Jan. 2024.

[14] G. Li, P. Shen, T.-W. Wong, *et al.*, "Plasticized electrohydraulic robot autopilots in the deep sea," *Sci. Robot.*, vol. 10, no. 105, eadt8054, Aug. 2025.

[15] T. Kim, J. Kim, and S.-C. Yu, "Development of bioinspired multimodal underwater robot "HERO-BLUE" for walking, swimming, and crawling," *IEEE Trans. Robot.*, vol. 40, pp. 1421–1438, 2024.

[16] K. Iguchi, T. Shimooka, S. Uchikai, *et al.*, "Agile robotic fish based on direct drive of continuum body," *npj Robot.*, vol. 2, no. 1, p. 7, Oct. 2024.

[17] Y. Zhong, Z. Li, and R. Du, "A Novel Robot Fish With Wire-Driven Active Body and Compliant Tail," *IEEE/ASME Trans. Mechatron.*, vol. 22, no. 4, pp. 1633–1643, Aug. 2017.

[18] C. Wang, V. R. Puranam, S. Misra, and V. K. Venkiteswaran, "A Snake-Inspired Multi-Segmented Magnetic Soft Robot Towards Medical Applications," *IEEE Robot. Autom. Lett.*, vol. 7, no. 2, pp. 5795–5802, Apr. 2022.

[19] X. Li, Z. Lin, and W. Ding, "Bio-inspired soft magnetic swimming robot for flexible motions," in *2025 IEEE International Conference on Robotics and Automation (ICRA)*, IEEE, May 19, 2025, pp. 15 343–15 349.

[20] R. Wang, C. Zhang, W. Tan, *et al.*, "Soft robotic fish actuated by bionic muscle with embedded sensing for self-adaptive multiple modes swimming," *IEEE Trans. Robot.*, vol. 41, pp. 1329–1345, 2025.

[21] D. Wei, S. Hu, Y. Zhou, *et al.*, "A magnetically actuated miniature robotic fish with the flexible tail fin," *IEEE Robot. Autom. Lett.*, pp. 1–8, 2023.

[22] R. Hennig, A. Beaudette, H. M. Golecki, and C. J. Walsh, "Educational soft underwater robot with an electromagnetic actuation," *Soft Robot.*, vol. 11, no. 3, pp. 444–452, Jun. 1, 2024.

[23] O. Yasa, Y. Toshimitsu, M. Y. Michelis, *et al.*, "An overview of soft robotics," *Annu. Rev. Control Robot. Auton. Syst.*, vol. 6, no. 1, pp. 1–29, May 3, 2023.

[24] M. Park, J. Cervera-Torralba, I. Adibnazari, G. Pawlak, and M. T. Tolley, "Analysis of kinematics and propulsion of a self-sensing multi-DoF undulating soft robotic fish," in *2025 IEEE International Conference on Robotics and Automation (ICRA)*, IEEE, May 19, 2025, pp. 14 692–14 692.

[25] X. Qi, H. Shi, T. Pinto, and X. Tan, "A Novel Pneumatic Soft Snake Robot Using Traveling-Wave Locomotion in Constrained Environments," *IEEE Robot. Autom. Lett.*, vol. 5, no. 2, pp. 1610–1617, Apr. 2020.

[26] T. Chen, X. Yang, B. Zhang, J. Li, J. Pan, and Y. Wang, "Scale-inspired programmable robotic structures with concurrent shape morphing and stiffness variation," *Sci. Robot.*, vol. 9, no. 92, eadl0307, Jul. 2024.

[27] X. Shi, Z. Chen, T. Zhang, *et al.*, "Hydrodynamic performance of a biomimetic undulating fin robot under different water conditions," *Ocean Eng.*, vol. 288, p. 116 068, Nov. 2023.